Experimental Thermal and Fluid Science 177 (2026) 111781

Contents lists available at ScienceDirect

Experimental Thermal and Fluid Science

journal homepage: www.elsevier.com/locate/etfs

Using a fast-response temperature-sensitive paint to spatially and temporally resolve transitional phenomena ☆

Benjamin Dimond *, Marco Costantini, Christian Klein

Institute of Aerodynamics and Flow Technology, German Aerospace Center (DLR), Bunsenstrasse 10, 37073 Göttingen, Germany

ARTICLE INFO

Keywords:
Laminar-turbulent transition
Temperature-sensitive paint
Turbulent spots
Heat-flux
Intermittency

ABSTRACT

Time-resolved temperature-sensitive paint is employed in this work to investigate transitional boundary layer phenomena on a flat plate model under high Reynolds number and high subsonic Mach number conditions. Spatially and temporally resolved surface heat flux distribution are inferred from the surface temperature evolution. The experiments are conducted at a Mach number of 0.8, high chord Reynolds numbers of 6 and 7.5 million, and under streamwise favourable pressure gradients with an acquisition frequency of 20 kHz. The bimodal distribution of surface heat flux enables the identification of laminar and turbulent boundary layer states, allowing for the direct determination of the time-dependent transition front and the time-averaged intermittency distribution. It is demonstrated, that conventional time-averaged transition detection methods — specifically, the location of maximum temperature gradient and peak temperature fluctuation — accurately correspond to the location of 50 % intermittency. Furthermore, the evolution of an isolated turbulent spot is spatially and temporally resolved and compared to hot-film traces.

1. Introduction

Understanding and predicting the length and location of laminar-turbulent transition remains of major importance in many engineering applications due to its significant impact on skin friction and heat transfer. For airfoils, the boundary layer state directly influences aerodynamic efficiency and performance, as the transition location affects surface friction and can influence flow separation [1]. Similarly, the transition location — and to a large extent the transition length — significantly affects heat transfer on gas turbine components (such as jet engine turbine blades) and hypersonic vehicles [2,3]. Accurately accounting for thermal loads and their spatial distribution in the design process can lead to substantial improvements in overall efficiency.

For most aerodynamic applications, the boundary layer starts laminar at the upstream part of a body and then becomes turbulent further downstream. Many parameters can influence if and where the boundary layer transitions from a laminar to a turbulent state, the most important of which are the Reynolds number, the properties and disturbance level of the free stream, the surface texture and the pressure gradient along the streamwise direction. The physical state of the boundary layer is characterized by the intermittency factor γ, defined as the fraction of time the flow is turbulent at a given spatial location. An intermittency factor of $\gamma = 0$ corresponds to fully laminar flow, and $\gamma = 1$ corresponds to fully turbulent flow. Generally, areas within the transition region are partly laminar and partly turbulent in time, resulting in an intermittency distribution. The stages of laminar-turbulent transition for a model flat plate flow are visualized in Fig. 1. It is important to note that the different areas are not sharply delimited and may vary considerably in size depending on the flow conditions. For a

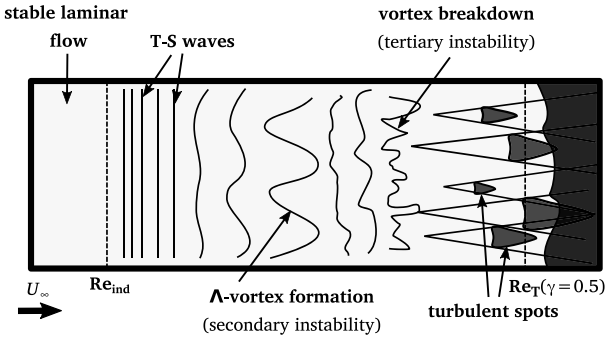

Fig. 1. Qualitative sketch of the laminar-turbulent transition process over a flat plate for a 2D flow (based on White [4]).

☆ This article is part of a Special issue entitled: 'ICEFM2025' published in Experimental Thermal and Fluid Science.

* Corresponding author.
E-mail address: benjamin.dimond@dlr.de (B. Dimond).

https://doi.org/10.1016/j.expthermflusci.2026.111781
Received 31 January 2026; Received in revised form 29 April 2026; Accepted 29 May 2026
Available online 3 June 2026

2D flow, disturbances within the boundary layer (T–S waves) grow in amplitude until they increase above a certain threshold. The two-dimensional structure of the disturbances breaks down, and Λ-vortices arise [5]. Experiments by Elder [6] showed that once the intensity of the disturbances grew large enough, turbulent spots emerged, with the flow properties inside of these spots resembling that of a fully turbulent boundary layer. Turbulent spots are generally idealized as downstream pointing triangles. They spread out in a wedge-shaped area and grow in stream- and spanwise direction as they propagate downstream where they eventually merge to form a fully turbulent boundary layer.

1.1. Aspects of laminar-turbulent transition

To model the stochastic transition process, several theoretical frameworks have been developed that describe the evolution of the intermittency γ — the fraction of time the flow is turbulent at a fixed location — based on the generation and propagation of turbulent spots. Based on a model of Emmons [7], it is possible to formulate a general intermittency distribution with respect to the streamwise distance x for a quasi-2D flow (intermittency distribution is the same along the spanwise coordinate y). The model assumes a "binary" boundary layer state, i.e., the boundary layer is either laminar or turbulent at a given position P at x, y at time t, and that transition occurs simply through the coalescence of turbulent spots. This is a simplification, as it does not account for intermediate flow conditions during breakdown and the state of the interface between laminar and turbulent portions. Emmons [7] showed that with this simplification the intermittency can be expressed as:

$$\gamma(P) = 1 - \exp\left[-\int_R g(P_0)\,\mathrm{d}V_0\right], \tag{1}$$

with a spot production function $g(P_0)$ (the probability of spot production at a point $P_0(x_0, y_0, t_0)$ per unit volume $\mathrm{d}V_0$) and R the dependence volume (spot sweep volume). R is assumed to be a cone with straight generators in the x, y, t volume, i.e., it has a constant spreading angle in space and time.

Due to a lack of better knowledge, Emmons suggested g to be a constant independent of x, i.e., the probability of spot generation is uniform along the surface. This proposition was later improved by Dhawan & Narasimha [8]. They proposed $g(x)$ to depend on the streamwise location x with a maximum at some location $x_{g,max}$. Assuming a Gaussian distribution, they found a best fit to experimental data with a standard deviation close to zero, i.e., close to a Dirac delta function $\delta(x)$. This represents a model of concentrated breakdown, where all turbulent spots arise within a narrow streamwise band. Several measurements have indicated that a Gaussian distribution fits experimental data better than a Dirac delta function [9,10]. However, the limiting case of a Dirac delta function is deemed sufficient if the region of spot production is small compared to the total transition length [2]. With $g(x) = n\delta(x_0 - x_{g,max})$ in Eq. (1), one obtains:

$$\gamma(x) = 1 - \exp\left[-(x - x_{g,max})^2 \frac{n\sigma}{U_\infty}\right], \tag{2}$$

with a turbulent spot production rate per unit length n, Emmons' dimensionless spot propagation parameter σ, and the freestream velocity U_∞. $\frac{n\sigma}{U_\infty}$ is assumed to be constant. For an idealized triangular shape of turbulent spots, the spot propagation parameter can be expressed as [11–13]:

$$\sigma = \left(\frac{1}{c_{te}} - \frac{1}{c_{le}}\right)\tan(\alpha), \tag{3}$$

where c_{le} and c_{te} are the leading and trailing edge celerity of individual spots, respectively. Introducing a dimensionless streamwise coordinate

$$\xi = \frac{x - x_{g,max}}{x_{75} - x_{25}}, \tag{4}$$

where x_{75} and x_{25} are the streamwise locations with intermittency $\gamma = 0.75$ and $\gamma = 0.25$, respectively, one obtains the Narasimha intermittency distribution [8,14,15]:

$$\gamma = 1 - e^{-\frac{(x - x_{g,max})^2 n\sigma}{U_\infty}} = 1 - e^{-0.411\xi^2}. \tag{5}$$

Because of the reasonably good agreement with experimentally observed intermittency distributions (e.g., Mee & Goyne [16], Owen [17]), Eq. (5) is often referred to as the "universal intermittency distribution" [14,16,18].

Johnson & Fashifar [19] alternatively assume the probability of turbulent spot generation to increase linearly with x. Solving the resulting differential equation, they obtain:

$$\gamma = 1 - e^{-0.0941\xi^3}. \tag{6}$$

Note the similarity to the Narasimha intermittency distribution of Eq. (5), but with ξ raised to the power of 3 instead of 2. This relation is phenomenologically similar to the empirical relation proposed by Abu-Ghannam & Shaw [20]. Both have demonstrated excellent correlation with experimental data [21,22].

1.2. Application of TSP for transitional studies

Despite extensive research so far, further investigation of the transition process is still needed, particularly for high Reynolds number flows which are relevant for commercial transport aircraft, where both numerical and experimental studies remain scarce. High Reynolds numbers pose challenges for measurement techniques due to small length scales in wind tunnel experiments and sensitivity to even minor disturbances, such as surface roughness [23,24]. One promising global, non-intrusive technique is temperature-sensitive paint (TSP), which enables quantitative, spatially resolved surface temperature measurements [25]. The underlying principle behind TSP lies in the temperature-dependent fluorescence properties of specific molecules known as luminophores, which are embedded within a polymer matrix. With incident light of a particular wavelength, photons are absorbed to excite the luminophore from the ground electronic state to an excited state [25]. They can return to the ground electronic state through different radiating (fluorescence and phosphorescence) and non-radiating processes. In general, the non-radiating process is more likely at higher temperatures through thermal quenching. Therefore, there is a inverse relationship between the temperature of the TSP and the intensity of the remaining radiating processes which allows for precise temperature reconstruction across the TSP coated surface. These measurements can be used to further obtain surface heat flux, which is directly related to the boundary layer state. While conventional TSP is well-established for steady or moderate-speed phenomena (sub-kHz regime) (e.g. [25–29]), unsteady measurements in the kHz regime (iTSP) are a fairly recent development [30–34].

The response time of TSP depends primarily on two factors: the luminescent lifetime of the luminophore and the thickness of the paint layer. The former must be short enough to resolve rapid temperature changes, while the latter must be minimized to reduce thermal inertia — since thermal inertia scales with the square of the layer thickness [35]. However, using thin layers requires high-energy excitation sources to achieve sufficient emission light intensity required for short exposure times. This, in turn, introduces new challenges such as photodegradation of the paint (irreversible loss of sensitivity and luminescence with accumulated excitation) and difficulties in achieving uniform illumination [24].

Over the past years, a few studies have employed iTSP to investigate unsteady transition phenomena. Petersen et al. [36] resolved unsteady transition and separation on an SiC/SiC nozzle guide vane with an environmental barrier coating at 10 kHz. Dimond et al. [37] used the same iTSP as that presented in this study to characterize the intermittent region of turbulent wedges and capture time-resolved

visualizations of individual turbulent spots. More recently, Yoshikawa and Ozawa [38] applied iTSP at frame rates up to 200 kHz to visualize and quantify heat flux traces from individual turbulent spots in hypersonic flow at $M = 5.2$. Liu et al. [34] used the same luminophore but embedded in a polyurethane clearcoat. Although the thickness was expected to be several dozen microns, an in-situ calibration allowed for the determination of heat-flux at a high sampling rate of 75 kHz in a shock tube at $M = 12.1$. In a completely different approach, Jung et al. [33] achieve a thin (<2 μm) phosphor-based TSP with ZnO:Zn particles with a ball-milling approach. Although the phosphorescent intensity decreased substantially because of the milling process, the thin layer enables a fast-response TSP with an inorganic TSP.

This study characterizes and applies time-resolved temperature-sensitive paint (iTSP) to investigate subsonic, compressible flows at high Reynolds numbers. It marks the first time that the mechanisms of laminar-turbulent transition could be temporally and spatially resolved with such a high resolution. The method leverages surface temperature measurements to infer temporally and spatially resolved heat flux, enabling high-fidelity reconstruction of transition phenomena, including intermittency evolution and individual turbulent spot dynamics. The work further extends the doctoral research of Dimond [24] and demonstrates the capability of iTSP to capture transient transition features with high temporal resolution.

2. Experimental setup

2.1. Cryogenic Ludwieg-Tube Göttingen

The experiments presented in this study were conducted in the low-turbulence Cryogenic Ludwieg-Tube Göttingen (KRG), which uses gaseous nitrogen as the test medium. During a run, the rapid gas expansion in the Ludwieg tube causes a significant temperature drop, resulting in a wall-to-adiabatic wall temperature ratio of $T_w/T_{aw} > 1$ [39,40]. By increasing the stagnation pressure (up to 10 MPa) and decreasing the gas temperature (down to 105 K), the facility enables testing at high Reynolds and Mach numbers. The test section measures 0.4 m in width, 0.35 m in height, and 2 m in length, with shaped upper and lower walls designed to minimize flow interference. The absence of moving parts, which are needed in other wind tunnel types for operating and regulating the flow, allows for good overall flow quality (mass flux density turbulence $Tu_{\rho u} \approx 0.06\,\%$ [39]). Further details about the wind tunnel and its instrumentation can be found in Refs. [39,41]. Note, that to accommodate the measurement technique (iTSP and camera) the wind tunnel is operated at near ambient temperatures (charge temperatures between 0 °C to 10 °C), while high Reynolds numbers were achieved by increasing the gas pressure. In this work, the Mach and Reynolds numbers are defined as freestream Mach number M based on the freestream velocity U_∞ and freestream speed of sound and chord Reynolds number $Re_c = U_\infty c/\nu_\infty$ based on test model chord length c with freestream kinematic viscosity ν.

2.2. Wind tunnel model

The experiments were performed using the 2D wind tunnel model *PaLASTra* [23,40]. The cross-sectional design, depicted in Fig. 2, ensures a uniform pressure gradient over a large streamwise area on the upper side of the model, especially in the region of interest, for a wide range of Mach numbers and angles of attack in the subsonic regime. The model has a width of $b = 500$ mm, a maximum thickness of 20 mm, and a chord length of $c = 200$ mm. The front part features a modified superellipse [42] as leading-edge surface to reduce receptivity to freestream disturbances. An additional aft part, not included in the original model version, reduces the size of the separation region and thus minimizes external disturbances to the boundary layer on the upper side [29]. The model was carefully assembled to ensure that no gap and/or step was present between the front and main parts of the model. Due to the extensive aerodynamic loads at KRG, small imperfections were measured after the tests (gap < 20 μm and forward-facing step < 3 μm), but these are not expected to affect laminar-turbulent transition for the investigated test cases.

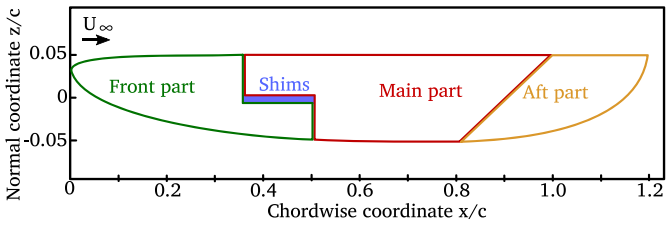

Fig. 2. Cross-sectional view of the *PaLASTra* test model. Chord length c = 200 mm.

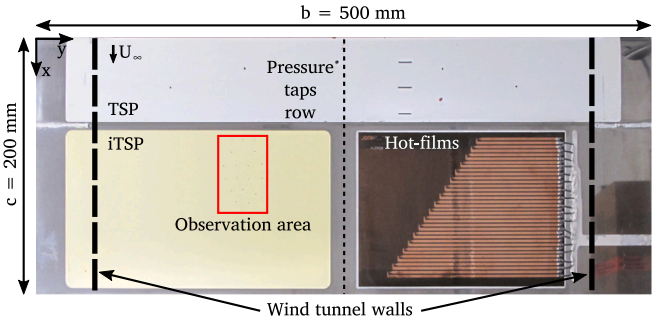

Fig. 3. Top plan view of the wind tunnel model (flow from the top). Aft part not visible in this image.

Fig. 3 shows a top plan view of the wind tunnel model with the wind tunnel wall locations indicated. The model features a total of 52 pressure taps distributed over the upper and lower surfaces, aligned along the centreline ($y/b = 0.5$). Two pressure taps are positioned at $y/b = 0.48$ to increase the spatial resolution at the leading edge region. The streamwise pressure gradient parameter used for this study is defined as

$$\lambda_\theta = \frac{\theta^2}{\nu}\frac{\mathrm{d}U_e}{\mathrm{d}x}, \tag{7}$$

with the kinematic viscosity ν. The momentum thickness θ and the boundary layer edge velocity gradient $\mathrm{d}U_e/\mathrm{d}x$ are determined with the boundary layer solver COCO for compressible flows [43] and averaged over the region of interest. The pressure gradient was controlled by adjusting the model's angle of attack using turntables mounted in the sidewalls of the test section.

The starboard side is equipped with a Senflex® multiple hot-film sensor array (MHFS) custom-designed and manufactured by Tao of Systems Integration, Inc. Eighteen hot-films are staggered at 35° to avoid influence from the leads and heat input of preceding sensors. They are equally spaced at 3 % chord length intervals, ranging from $x/c = 41\,\%$ to $x/c = 92\,\%$ and covering the main region of uniform pressure gradient. The sensors consist of a thin nickel layer (1.45 mm wide, 0.1 mm streamwise, 0.2 μm thick) with copper leads of 5 μm thickness. The leads are connected to custom-designed in-house constant-temperature anemometers (CTA) [39]. The sensors were operated at an overheat ratio (OR) of $\frac{R_S}{R_0} = 1.4$, where R_S and R_0 are the resistance at the operating level and ambient condition, respectively. Before every data point, the anemometers were experimentally checked and confirmed to have a frequency response of at least 50 kHz using a square-wave test. The analogue output of each anemometer was recorded with a separate digital data acquisition system (YOKOGAWA® SL 1000) with a sampling frequency of 1 MHz and resolution of 16 bit.

Two areas are coated with TSP: the front part including the leading edge, and the port side of the main part. The front part uses the same TSP from previous investigations [23,27,40,44], which has an europium (Eu) complex as luminophore [45] and is applied in a pocket to match the required model contour. It was sanded to $R_a = 0.033(2)\,\mu m$ and extends to 5 % of the chord on the lower surface. This Eu-based TSP is not suitable for highly time-resolved measurements but had been used previously to detect turbulent wedges at the leading edge region. The port side of the main part is coated with iTSP, which is discussed in detail in the following section. It covers a chordwise region from 36.5 % to 97.5 % on the upper surface, and is also applied in a pocket. No TSP is applied around the model junction (between the TSP and iTSP coated surfaces) to ensure surface smoothness in this area. Because both the TSP and iTSP coatings are embedded in pockets, the interface between the areas remain smooth and are not expected to influence the boundary layer. The aft part, whose sole purpose is to reduce the separation region as discussed above, remained uncoated.

Felt tip markers were applied within the observation area of the model. They were used to map the camera image coordinates to 3D model coordinates and to correct for vibrations and displacement during the run using the in-house software package *ToPas* [46].

2.3. iTSP properties

The temperature-sensitive paint used for this investigation, capable of measuring surface temperatures with high temporal resolution (iTSP), uses Dichlorotris (1,10-phenanthroline) ruthenium (II) hydrate (98%) (Ru(phen)) as luminophore, which has a very short luminescent lifetime of less than 1 µs [47]. It is embedded in an ethanol-soluble polyamide binder at a luminophore concentration of 0.16 mol/L based on the binder density. Both components are dissolved in ethanol and the solution is spray-coated onto the model. Similar iTSP formulations with different concentrations have been used in previous studies [30, 48–50]. The total paint setup consists of three layers: a thin primer layer (approx. 20 µm) to provide better adhesion to the metallic surface; a thick white base layer (approx. 100 µm) for thermal insulation and to create a diffusive light-reflecting background; and finally the active layer (less than 1 µm thickness) mentioned above. The thickness of the active layer was estimated to be between 0.3 µm to 0.8 µm, based on surface profilometer measurements and geometric considerations of the amount of applied paint.

The sensitivity of the iTSP is determined in a calibration chamber, where temperature and pressure can be set individually. Details on setup and properties of the chamber can be found in Ref. [51]. A small calibration sample (an aluminium plate) with dimension 15 mm by 15 mm is coated at the same time as the model to ensure that the coating has the same paint composition and thickness.

The relative intensity and sensitivity of the iTSP can be seen in Fig. 4. The paint has a very high temperature sensitivity of around $S = -5\,\%/\mathrm{K}$, where S is defined as

$$S = \frac{(I_+ - I_-)\cdot 100}{(I_+ + I_-)/2\cdot(2\Delta T)}, \tag{8}$$

with $I_- = I_{T-\Delta T}$ and $I_+ = I_{T+\Delta T}$ being the intensity values at temperatures $T - \Delta T$ and $T + \Delta T$, respectively. Since the experiments were conducted in a nitrogen environment without oxygen, the (weak) pressure sensitivity of this iTSP had no influence on the results. Unfortunately, this iTSP is sensitive to photodegradation (see Section 1). Extensive illumination can reduce the intensity emitted by the iTSP by over 80 % and the sensitivity by over 50 %. Further information on the photodegradation is provided in Ref. [24]. Great care must be taken to expose the iTSP to as little excitation light as possible to minimize the effect of photodegradation. However, during the measurement campaign it could not be completely avoided and must be accounted for, as described in Section 3.1.

The excitation and emission spectrum of the iTSP can be seen in Fig. 5. Seven high-power blue LEDs (4x LED ENGIN LZ4-00DB00 and 3x OSRAM LE B P3W with similar spectra) are used to excite the iTSP, as sketched in Fig. 6. They are fitted with Chroma® ET470/40x or ET450/50x bandbass optical filters to exclude any possible red light from the LEDs to reach the iTSP surface. Two of the LEDs are additionally equipped with 50 mm lenses to focus the light on to the surface of interest.

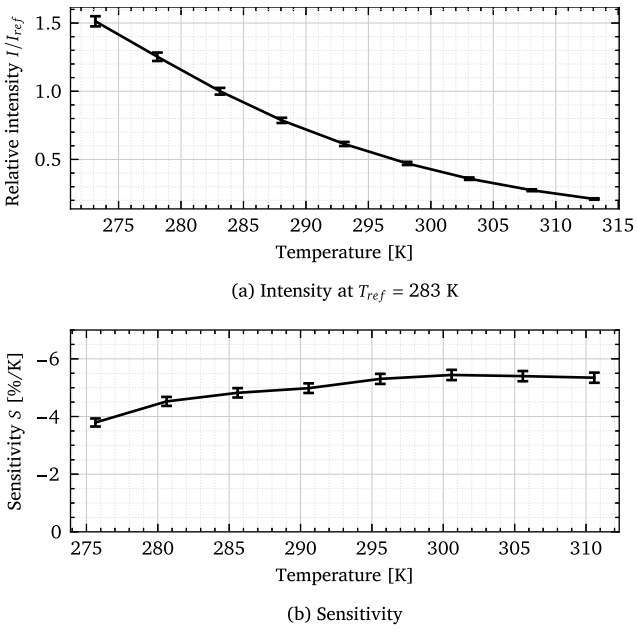

(a) Intensity at $T_{ref} = 283$ K

(b) Sensitivity

Fig. 4. (a) Relative intensity (error bars are multiplied with a factor of ten for better visibility) and (b) Sensitivity of the iTSP in the relevant temperature range.

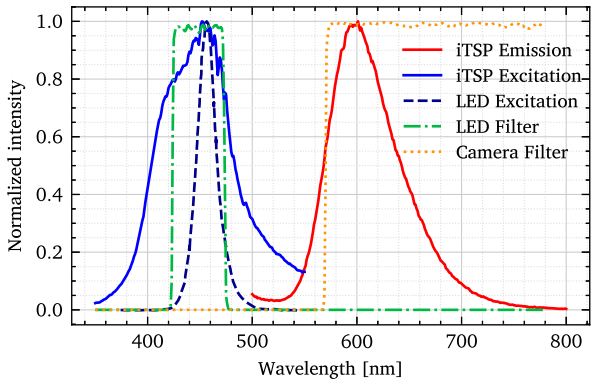

Fig. 5. Emission and excitation spectra for iTSP at $T = 283$ K, LED spectrum and transmission spectra of the LED (OSRAM LE B P3W) and camera filters.

A Photron® Fastcam Mini AX200 high-speed camera is used to capture the iTSP intensity images. It features a 1-megapixel (1024 × 1024 px^2) CMOS image sensor with a global shutter and 12-bit dynamic range. Due to its compact build and suitability for applications in high-G environments (which can occur in KRG due to the vibrations during operation), it is well suited for this investigation. The camera is operated at 20 kHz at a recording resolution of 1024 × 256 px^2. A Scheimpflug adaptor is used to increase the depth-of-field focus. An 85 mm f/1.4 Nikkon lens is combined with a macro extender to allow focusing to the short distances. The lens must be set at full aperture

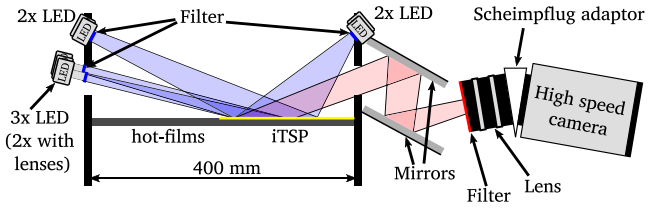

Fig. 6. Schematic of the iTSP measurement setup. View is in the streamwise direction.

to ensure the camera detects sufficient luminescent light. The resulting loss in depth-of-field focus was tolerable as the images needed to be strongly filtered anyhow. Two mirrors are used in a periscope setup to enable a view of the region of interest, especially in this spatially constricted environment. A similar setup had been used and described by Risius et al. [29,52,53] and adapted for the current investigation. This setup and the lens enabled a very high streamwise resolution of 17 px/mm for the 55 × 32 mm^2 observation area (see Fig. 3). The camera is fitted with a Chroma® ET570lp long pass optical filter to capture a large part of the relatively broad emission peak of the iTSP (compare Fig. 5).

3. Data processing

3.1. Calibration procedure

As described in section 2.3, prolonged illumination induces irreversible photodegradation of the iTSP, which must be accounted for when determining quantitative surface temperatures. Consequently, the conventional approach of relying solely on a calibration curve obtained in a separate calibration chamber [25] is not feasible in this setup. Furthermore, the illumination distribution within the test section is not fully uniform, resulting in spatially varying degradation rates across the model surface. Given the significant effort required to mount and dismount the model and optical setup, it was impractical to recoat the model after every few test runs.

To enable quantitative temperature measurements despite photodegradation, a multi-step procedure was developed. This approach minimizes light exposure, performs in-situ calibration of the iTSP on the model before and after each test campaign, and applies an external calibration to correct the in-situ results.

Great care was taken to reduce light exposure during model installation, including pre-alignment of the optical setup. During tests, the LED on-time was limited to 1.5 s to minimize thermal and photodegradative effects. However, even this short duration caused a decay in LED intensity during the run due to incomplete thermal equilibrium, which was corrected using a third-order polynomial fit.

The test facility allowed temperature variation within the test section, enabling in-situ calibration. Because the LEDs were also exposed to the temperature changes, their output intensity also varied, so the sensitivity derived from the in-situ measurements was overestimated. To correct for this, the in-situ calibration was adjusted by scaling the measured intensities so that the resulting sensitivities matched those obtained from the external calibration. This adjustment assumes that, at the start of the test campaign, the in-situ and external calibrations would give identical calibration curves. Fig. 7 shows the measured sensitivities at 283 K for the examined area at the start and at the end of the test campaign. The differing sensitivities observed at the end of the campaign arise from variations in the photodegradation rate caused by paint inhomogeneities, non-uniform illumination intensities, and differences in paint thickness. Given that the overall sensitivity loss was relatively small (10 % to 20 %), a linear interpolation between the corrected in-situ calibration results obtained at different times during

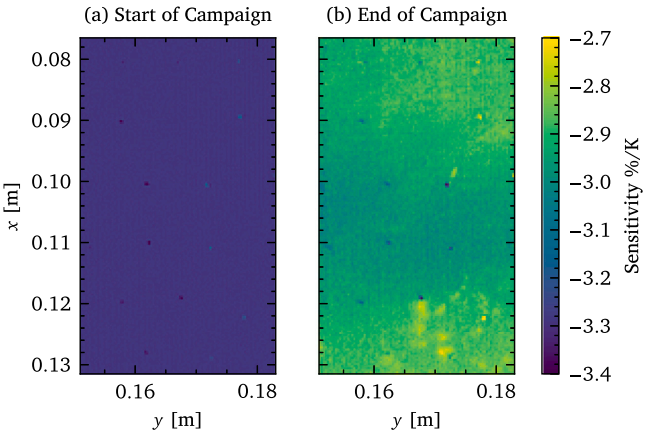

Fig. 7. Sensitivities on the area of interest at 283 K at the start and end of the test campaign.

the test campaign was applied. The interpolation weights were based on the relative position of each data point within the test campaign, effectively accounting for spatial variations in photodegradation due to different illumination intensities, location on the model, and paint inhomogeneities.

After mapping the images to model coordinates and computing surface temperatures using the above procedure, the data were filtered to enhance the signal-to-noise ratio. A Gaussian spatial filter with a streamwise-to-spanwise ratio of 4:1 was applied, which corresponds to a kernel size of 1.2 mm by 0.3 mm on the grid and covers about 20 × 2 px^2. Additionally, a Savitzky–Golay temporal filter was used: a second-order polynomial was fitted to a sliding window of five consecutive time instances, and the filtered value was evaluated at the central time point, consistent with the average peak width observed in the data. This filter was chosen, as it better preserves peak width and height compared to other filters.

3.2. Heat flux determination

The time-dependent heat flux distribution on the surface gives a direct indication of the boundary layer state, with a turbulent boundary layer yielding a higher heat flux compared to a laminar boundary layer, assuming the temperature difference between T_{aw} and T_w to be similar in both cases. Based on the assumptions listed below, the heat flux can be calculated with the time-resolved, surface temperature distribution measured by the iTSP and the thermal properties of the iTSP layers and wind tunnel model.

For a 1D heat transfer, which is a common approximation in short-duration wind tunnels [31,35,48,54–56], the time-dependent temperature distribution along an axis z is determined by [57]

$$\rho(z,T)c(z,T)\frac{\partial T}{\partial t} = \frac{\partial}{\partial z}\left(k(z,T)\frac{\partial T}{\partial z}\right), \tag{9}$$

a parabolic partial differential equation with temperature T, thermal conductivity k, density ρ and specific heat capacity c. At any given position, the heat transfer is given by (Fourier's law) [57]

$$\dot{q}(t) = -k\frac{\partial T(t)}{\partial z}. \tag{10}$$

These equations can be used to calculate the heat flux on the surface of the wind tunnel model coating $\dot{q}_w(t) = -k\frac{\partial T(t)}{\partial z}|_{z=z_w}$ with $z_w = z_0$ the surface location. Before every run, the temperature is assumed to be constant throughout the model, which is a reasonable assumption for a blow-down tunnel with long equilibration times between runs, and its absolute value is determined by thermocouples in the model and the

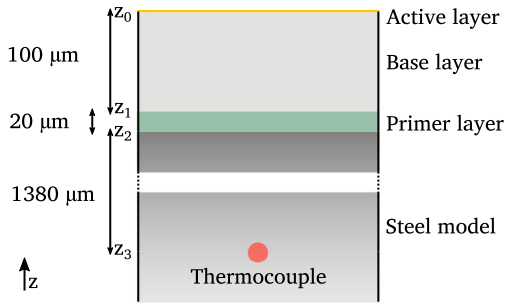

Fig. 8. Layer model of the iTSP with approximate thicknesses.

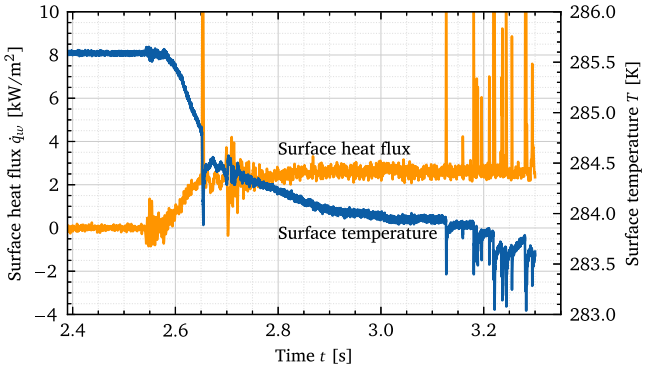

Fig. 9. Calculated heat flux and the temporal temperature distribution at $x = 0.1\,\text{m}$, $y = 0.167\,\text{m}$ for $Re_c = 6 \cdot 10^6$, $M = 0.8$, and $\lambda_\theta = 19.0 \cdot 10^{-3}$.

test section. The time-dependent temperature distribution is acquired by iTSP as discussed in Section 2.3.

In general, the thermal properties of a material varies with temperature. Since the total temperature change is small in this investigation (change of surface temperature measured to be $< 6\,\text{K}$ for all cases), the thermal properties of the iTSP layers and model are assumed to be constant with respect to temperature, i.e. $\rho(z,T) = \rho(z)$, $c(z,T) = c(z)$, and $k(z,T) = k(z)$. Furthermore, the change of these properties with respect to z is assumed to be constant within one material layer and only varies at the layer intersections (piecewise constant) — compare with Fig. 8. Further details on the numerical calculation are given in Appendix A.

For the heat flux determination, the images were binned to a grid with 137 × 80 grid points (2.5 grid points per mm for the observation area) and further filtered with an additional Gaussian filter with kernel size 3 × 1 (corresponds to $1.2 \times 0.4\,\text{mm}^2$) in a streamwise direction to achieve a sufficient signal-to-noise ratio for the heat flux calculation. The calculated heat flux and temperature distribution for a predominantly laminar boundary layer are presented in Fig. 9. The heat flux values are filtered with a running Gaussian filter in time (kernel size 5). Towards the end of the run (at $t = 3.1\,\text{s}$ to $3.3\,\text{s}$), the spikes in temperature and heat flux are caused by turbulent spots, the last one of which close to $t = 3.3\,\text{s}$ corresponds to the turbulent spot which will be discussed further in Section 4.2. They predominantly appear towards the end of the steady test time when the turbulence level of the freestream increases slightly [24,39]. The surface temperature at around $3.0\,\text{s}$ and consequently the wall temperature ratio T_w/T_{aw} are close to constant, inferring an expected constant heat flux. The determined heat flux is constant for most of the run, demonstrating the validity for the choice of the thermal parameters. Further remarks on the heat flux determination and a comparison with the semi-infinite approximation typical for short-duration wind tunnels [31,35,54] are given in [24].

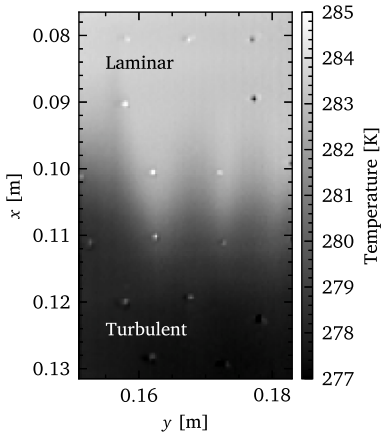

Fig. 10. Temperature distribution averaged for $3.0\,\text{s} < t < 3.1\,\text{s}$. Flow conditions are $Re_c = 7.5 \cdot 10^6$, $M = 0.8$, and $\lambda_\theta = 12.9 \cdot 10^{-3}$.

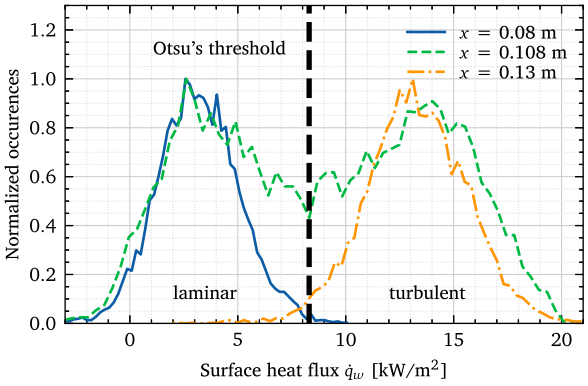

Fig. 11. Heat flux distribution for three streamwise positions at $y = 0.169\,\text{m}$ for $3.0\,\text{s} < t < 3.1\,\text{s}$. The time-resolved heat flux distribution corresponding to these conditions is given in supplementary video 1. Flow conditions are $Re_c = 7.5 \cdot 10^6$, $M = 0.8$, and $\lambda_\theta = 12.9 \cdot 10^{-3}$.

3.3. Determination of intermittency

With the high temporal resolution of the surface temperature measurements by means of iTSP, it is possible to directly determine the intermittency factor γ of the boundary layer for every location. Fig. 10 shows the average surface temperature distribution for $Re_c = 7.5 \cdot 10^6$, $M = 0.8$, and $\lambda_\theta = 12.9 \cdot 10^{-3}$ — a case where the flow transitions from fully laminar to fully turbulent within the field of view.

Fig. 11 presents histograms of the calculated surface heat flux at three streamwise locations — $x = 0.08\,\text{m}$, $x = 0.108\,\text{m}$, and $x = 0.13\,\text{m}$ — at a fixed spanwise position of $y = 0.169\,\text{m}$. These locations correspond to fully laminar, transitional, and fully turbulent boundary layer conditions, respectively. The level of the heat flux is determined by the heat transfer coefficient and the temperature difference between the wall and the adiabatic wall temperature. For all test cases considered here, the adiabatic wall temperature is lower than the wall temperature, resulting in a net energy transfer from the surface to the flow regardless of the boundary layer state.

A nearly binary separation is evident in the heat flux distributions, with lower heat flux values corresponding to laminar flow and higher values to turbulent flow. To categorize the instantaneous heat flux measurements objectively, Otsu's method [58] is applied. This non-parametric technique, widely used in image processing, identifies a robust threshold for bimodal data by minimizing the intra-class variance across all possible threshold values. Applying Otsu's method to

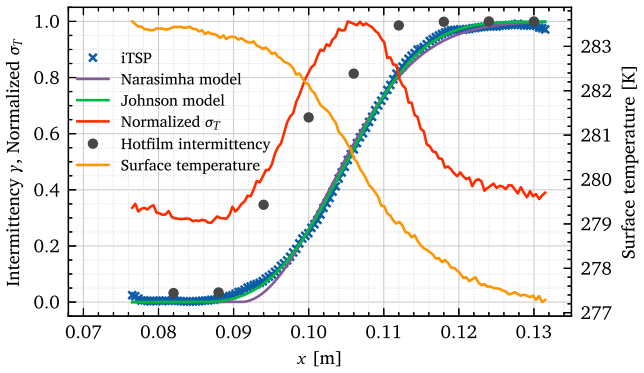

Fig. 12. Comparison of intermittency distribution with surface temperature and σ_T for $3.0\,\mathrm{s} < t < 3.1\,\mathrm{s}$ at $y = 0.169\,\mathrm{m}$. Flow conditions are $Re_c = 7.5 \cdot 10^6$, $M = 0.8$, and $\lambda_\theta = 12.9 \cdot 10^{-3}$.

all instantaneous heat flux measurements yields a threshold value of $\dot{q}_w = 8.3\,\mathrm{kW/m^2}$. Using this threshold, the boundary layer state is classified binary as either laminar or turbulent. The evaluation time interval is restricted to $3.0\,\mathrm{s} < t < 3.1\,\mathrm{s}$, during which the flow conditions are stable but before additional turbulent spots, caused by a higher turbulence level of the freestream, begin to appear in the upstream laminar region. A video of the surface heat flux transition region at the middle of the evaluation time ($t_0 = 3.05\,\mathrm{s}$) is presented in supplementary video 1. It demonstrates the high-frequency dynamics of the transition process over a large streamwise area with sudden bursts of turbulent areas (turbulent spots).

Since a calibration of the hot-film data to achieve quantitative wall shear stress information is particularly challenging for a compressible flow, the concept of quasi wall shear stress is used, as introduced by Hodson et al. [59] and utilized by Braune and Koch [60]. It is based on the connection between the heat transfer (from hot film to flow) to local wall shear stress according to the Reynolds analogy. As the hot-films are operated in constant temperature mode (keeping the resistance R constant), the quasi wall shear stress can be calculated with

$$\tau_q := \left(\frac{U(t)^2 - U_0^2}{U_0^2} \right)^3, \tag{11}$$

with $U(t)$ the voltage during a run and U_0 the voltage without flow required to keep a constant temperature of the hot-films. Although not directly proportional to the wall shear stress, the quasi wall shear stress behaves in a similar way and is deemed sufficient for the purposes of this study ($\tau_q = h(\tau_w)$ with a monotonous function h that is close to linear). To further determine the intermittency, a similar procedure to the one described in Clark et al. [61] was used, which was also utilized in several other studies. A detector function is defined as $D_i = m\tau_{q,i}'^2$ with m the relative magnitude of the signal $m = (\tau_{q,i} - \tau_{q,min})/(\tau_{q,max} - \tau_{q,min})$ and τ_q' the gradient of τ_q, with $\tau_{q,i}$ the quasi wall shear stress at time instance i. This detector function is smoothed with an exponential function with time constant $7\,\mu\mathrm{s}$ and thresholded with a selected value of $1 \cdot 10^{-8}$ to attain a binary time series — 0 for a laminar and 1 for a turbulent boundary layer. The threshold value was carefully chosen and did not significantly influence the results presented below. The advantage of using a detector function compared to the quasi wall shear stress alone is that it also accounts for fluctuations associated with a turbulent boundary layer.

4. Results and discussion

4.1. Laminar turbulent transition

The intermittency factors calculated are presented in Fig. 12, alongside the results based on the Narasimha [8,14,15] and Johnson [19] intermittency models (which will be labelled in this study as *Narasimha* and *Johnson* models, respectively), the surface temperature, a normalized σ_T distribution and the intermittency factors determined by the hot-films. It must be emphasized that the iTSP intermittency distribution results from a *direct* determination of time-resolved laminar and turbulent periods and does not rely on time-averaged quantities, as is often utilized in these flow conditions for thermal imaging.

Fig. 11 shows an overlap in the heat flux values associated with laminar and turbulent flow. This overlap arises from random noise in the signal and limited temporal resolution. This means some values of surface heat flux cannot be clearly associated with a laminar or turbulent boundary layer and may be falsely associated. For regions near $\gamma = 0.5$, the effects of false detections are expected to cancel each other out. Only near the fully laminar and fully turbulent regions is the distribution slightly compressed, since values falsely associated to a certain boundary layer state will prevent the distribution from reaching exactly 0 (for laminar flow) or 1 (for turbulent flow). However, this effect is small in the present case due to the high Mach number, which results in a high signal-to-noise ratio. The artifacts observed near the leading and trailing edges of the iTSP region ($x < 0.078\,\mathrm{m}$ and $x > 0.130\,\mathrm{m}$) in Fig. 12 are caused by a decreased signal-to-noise ratio toward the edges. The Johnson and Narasimha models in Fig. 12 are fitted with a least-square algorithm to estimate the transition onset and length. The Narasimha model underestimates the distribution for values close to 0 and 1 but shows a reasonable agreement in the intermediate part. On the other hand, the Johnson model shows a good agreement throughout the distribution and seems a better model for this investigated test case. As opposed to the model of concentrated breakdown as the basis for the Narasimha model that leads to an abrupt start but comparably smooth ending of the intermittency levels, the Johnson model, which is based on a streamwise distribution of turbulent spot initiation points, starts more smoothly. This assumption is more appropriate for the environment of KRG (and wind tunnels in general) where the disturbance levels are not uniform in time. Their amplification will, therefore, lead to laminar-turbulent breakdown in different streamwise locations.

The intermittency values determined with the hot-films show a similar distribution but with a transition further upstream. (Note the intermittency value of hot-film sensor #5 at $x = 0.106\,\mathrm{m}$ is questionable since this hot-film sensor did not function reliably during the measurement campaign.) This discrepancy of an upstream shifted intermittency distribution could be caused by small surface imperfections related to the hot-film foil and its installation in the wind tunnel model. As shown in Fig. 13(a), the transition location is not uniform in the spanwise direction. Since the hot-films are staggered in a spanwise direction, each sensor is associated with a different transition location, making the interpretation of transition length and shape more challenging.

4.1.1. Standard deviation of iTSP temperature distributions

A further way to quantify laminar-turbulent transition is to investigate the standard deviation of the surface temperature distribution in time σ_T (compare Miozzi et al. [28] and Ashill et al. [62]). This method has the benefit of not needing to compute the heat flux, but instead utilizing the directly measured quantity of surface temperature. For every streamwise location, the standard deviation of the mean of the surface temperature time series is calculated. Fig. 12 shows the σ_T distribution normalized with the maximum detected σ_T value. The σ_T value is higher for the transitional region compared to areas associated with fully laminar and fully turbulent flow, which is due to the fast drops in surface temperature due to turbulent spots and subsequent recovery during passages of laminar flow. The intermittency factor is expected to be close to 0.5 at the maximum of the σ_T value, which relies on the assumption that the turbulent spots are equally distributed [63–65].

The σ_T value is higher in the fully turbulent area than in the fully laminar area. One must be cautious with the interpretation as these areas are associated with different surface temperatures and temperature

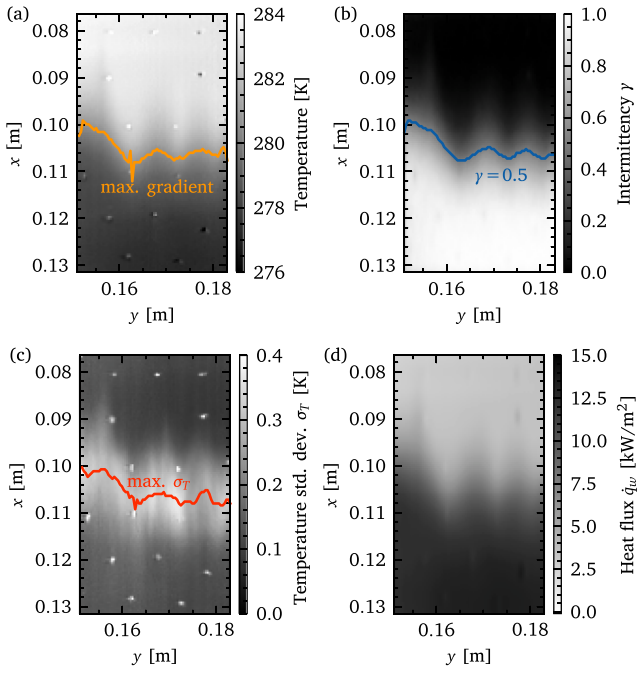

Fig. 13. (a) Comparison of surface temperature distribution, (b) intermittency distribution, (c) standard deviation of temperature σ_T, and (d) average heat flux $\dot{q}_w$, along with the corresponding detected transition locations for (a)–(c). A direct comparison of transition locations can be seen in Fig. 14. Time span is $3.0\,\mathrm{s} < t < 3.1\,\mathrm{s}$ with flow conditions $Re_c = 7.5 \cdot 10^6$, $M = 0.8$, and $\lambda_\theta = 12.9 \cdot 10^{-3}$.

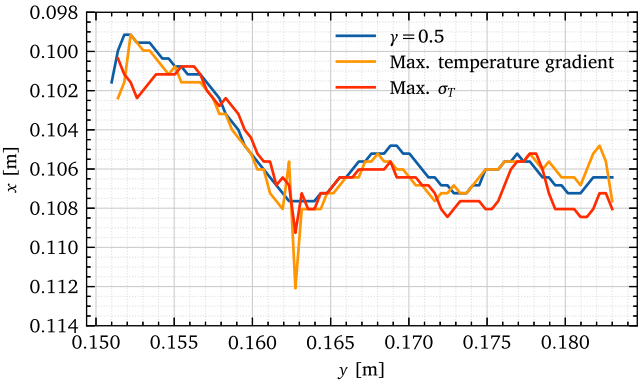

Fig. 14. Detected transition locations for the direct intermittency determination, maximum temperature gradient and maximum σ_T for $3.0\,\mathrm{s} < t < 3.1\,\mathrm{s}$ with flow conditions $Re_c = 7.5 \cdot 10^6$, $M = 0.8$, and $\lambda_\theta = 12.9 \cdot 10^{-3}$.

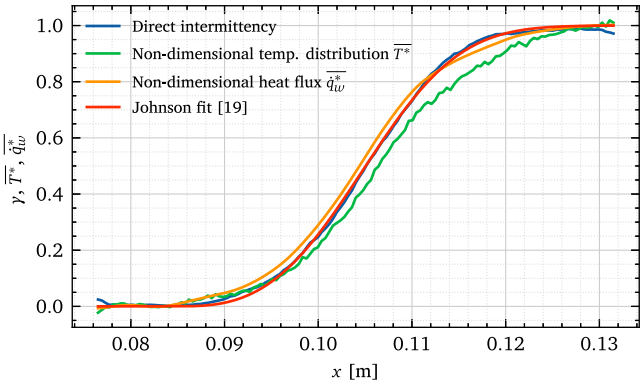

Fig. 15. Intermittency distribution and non-dimensional temperature and heat flux distribution for $3.0\,\mathrm{s} \leq t \leq 3.1\,\mathrm{s}$ at $y = 0.169\,\mathrm{m}$ with flow conditions $Re_c = 7.5 \cdot 10^6$, $M = 0.8$, and $\lambda_\theta = 12.9 \cdot 10^{-3}$.

gradients inside the model. Still, it suggests that the turbulent structures that cause a large variation in convective heat flux lead to the larger standard deviation of the σ_T value.

4.1.2. Surface temperature distribution

Due to the increased heat flux associated with a turbulent flow and the ratio between model surface temperature and adiabatic wall temperature T_w/T_{aw} being larger than one, the surface temperature decreases from a laminar to a turbulent boundary layer. This relationship is often used to reliably define a transition location [63] as the location of the highest streamwise temperature gradient. To determine this location, the procedure described in Costantini et al. [63] serves as a basis and is applied to every spanwise position. The temperature signal is filtered in space with a uniform filter and a subsequent Gaussian filter, both with kernel size of 5 %. The maximum gradient that lies within 20 % to 80 % of the minimum and maximum recorded temperature is identified as the transition location.

The aforementioned quantities (maximum temperature gradient, intermittency distribution, and temperature standard deviation) and the averaged heat flux are presented in Fig. 13 for the investigated surface area. Furthermore, the transition locations obtained using the three methods are shown and directly compared in Fig. 14. All three methods show remarkable agreement, with the variation between the locations detected by these methods being much smaller than the spanwise variations of the transition itself. The transition front is not a straight line but appears frayed, this being a consequence of a natural transition front for which instabilities are amplified [26,29,40]. Spanwise variations in the model contour, of the surface roughness in the leading edge region and in the freestream properties may lead to different amplifications of boundary layer disturbances, thus causing transition onset and extent to vary in the spanwise direction. The total variation, in this case, is about 4 % of the chord length and is caused by the upstream transition in the region $y = 0.15\,\mathrm{m}$ to $0.16\,\mathrm{m}$. It is probably caused by a surface defect in the leading edge region or close to the iTSP surface. In fact, when applying the active layer (see Section 2), the regions that are not meant to be coated are masked with masking tape. When it is removed, occasionally, the interface between areas without and areas with an active layer may not be perfectly smooth. Although the total thickness of the active layer is below 1 µm, this could be much larger at the edges if the paint runs up the masking tape. Therefore, the edges were carefully treated to remove large irregularities. Because the active layer of the iTSP cannot be sanded conventionally, some smaller irregularities might still persist, causing a transition further upstream for the high Reynolds number cases. (This aforementioned defect, however, could not be identified upon visual inspection after the test campaign.)

For the spanwise region $y = 0.16\,\mathrm{m}$ to $0.18\,\mathrm{m}$ the variation in transition location is much smaller, being around 1 %. For both the σ_T value and the maximum temperature gradient, the measured locations are influenced by interference from the presence of the marker located at $y = 0.163\,\mathrm{m}$; this has a great influence on the measured surface temperature and cannot be fully compensated for (compare Section 2.3). There is only a minor influence of the markers on the determined intermittency distribution and heat flux (compare Figs. 13(b) and 13(d)) or on the properties of the turbulent spots.

The streamwise evolution of the boundary layer condition can further be evaluated with a non-dimensional average surface temperature and average heat flux distribution. The non-dimensional temperature

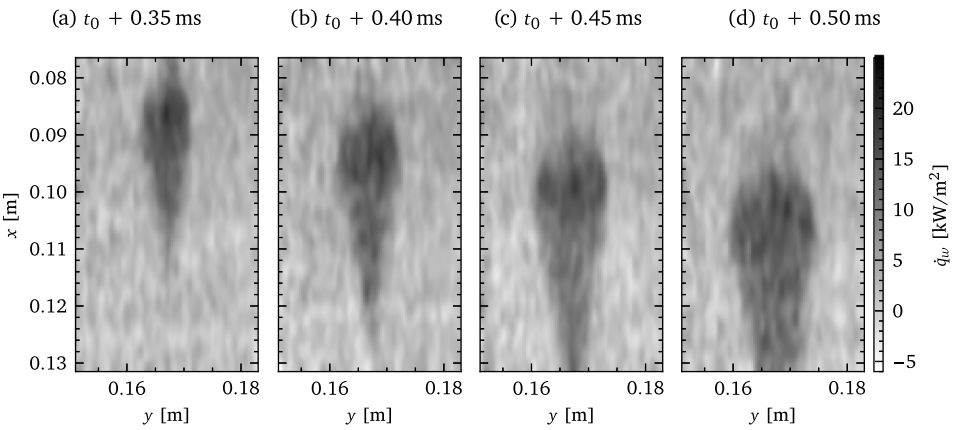

Fig. 16. Surface heat flux distribution for an isolated turbulent spot with $Re_c = 6 \cdot 10^6$, $M = 0.8$, and $\lambda_\theta = 19.0 \cdot 10^{-3}$ at $t = 3.2944$ s. A video of the presented spot passage is presented in supplementary video 2. Flow is from top to bottom.

distribution is defined here as

$$T^* = \frac{T - T_{lam}}{T_{tur} - T_{lam}} \tag{12}$$

and $\overline{T^*}$ is T^* averaged over the respective time span. T_{lam} and T_{tur} are calculated as an average over the respective time span of the first and last ten grid points ($0.0765\,\text{m} < x_{lam} < 0.0805\,\text{m}$ and $0.1275\,\text{m} < x_{tur} < 0.1315\,\text{m}$) respectively, where the boundary layer is expected to be fully laminar or fully turbulent. Accordingly, a non-dimensional heat flux can be defined analogously as

$$\dot{q}_w^* = \frac{\dot{q}_w - \dot{q}_{w,lam}}{\dot{q}_{w,tur} - \dot{q}_{w,lam}} \tag{13}$$

with the average laminar and turbulent heat flux $\dot{q}_{w,lam}$ and $\dot{q}_{w,tur}$ and the average value $\overline{\dot{q}_w^*}$ calculated as above. According to Dhawan & Narasimha [8] and Chen & Thyson [66], the non-dimensional time-averaged heat flux is equivalent to the intermittency distribution. Contrary to their proposal, the laminar and turbulent heat flux level is taken to be constant here rather than as function of the streamwise coordinate. Evaluating flow conditions that result in a fully turbulent or laminar boundary layer for the field-of-view yielded only a small streamwise change in surface heat flux, within the uncertainty range of the present measurement technique. The non-dimensional temperature and non-dimensional heat flux distributions are presented in Fig. 15 along with the direct intermittency and the corresponding fitted Johnson distribution. The averaged surface temperature is well below the intermittency curve for the latter stages of transition; this is considered to be due to the specific working principle of KRG. When the flow is established in the early stages of the run, the transition location moves upstream until it reaches a quasi-steady state for the remainder of the run. Therefore, the regions far downstream will generally be cooler compared to turbulent regions closer to the transition region, since there was a longer time span with a high heat flux to cool the iTSP and the underlying layers. Using the streamwise temperature distribution to detect the onset and end location of the transition region (like presented by Weiss et al. [67]) depends on the temperature history, and may therefore be unreliable in this case or in generall cases with a moving transition front. In contrast, the detected transition location (corresponding to 50% intermittency — determined via the maximum surface temperature gradient method) is reliable in this case and shows good agreement with the other techniques.

4.2. Turbulent spots

4.2.1. Turbulent spot traces

Fig. 16 shows the surface heat flux distribution for an isolated turbulent spot with $Re_c = 6 \cdot 10^6$, $M = 0.8$, and $\lambda_\theta = 19.0 \cdot 10^{-3}$ recorded at 20 kHz. A video of the spot passage corresponding to the snapshots provided in Fig. 16 is provided in supplementary video 2. Note, that in contrast to many previous studies, this turbulent spot is not artificially created but is a naturally occurring spot. It originates upstream of the observation area through the interaction of freestream turbulence and model surface and grows in a streamwise and spanwise direction as it propagates downstream. The presented turbulent spot is one of many isolated turbulent spots found throughout the measurement campaign. The properties and interactions between each other are further discussed in more detail in Dimond [24]. In this case, the heat flux is representative of the convective heat-transfer coefficient since the temperature difference between wall temperature and adiabatic wall temperature is essentially close to constant throughout the passage of the spot. The heat flux is, therefore, a direct representation of the state of the boundary layer. The general downstream-pointing triangular shape is visible. The leading edge tip is seen to be pointed, at least within the limitations of the image resolution. The wing tips of the turbulent spot are rounded, in contradistinction to the idealized triangular shape. This effect has also been observed in numerical calculations for supersonic flows [18,68]. The trailing edge interface is mostly flat, but with some bulges.

There is only a faint appearance of a calmed region on the heat flux level that can be seen trailing the turbulent spot in Fig. 16. A better visualization is given in Fig. 17: There is an area of increased heat flux compared to the values observed in the purely laminar boundary layer between $0.08\,\text{m} \leq x \leq 0.10\,\text{m}$. The calmed region is expected to span about the same duration as the turbulent spot itself [69] and, therefore, should cover a significant streamwise portion in images 16(b) to 16(d). Van Hest et al. [70] stated the length to be between one- and two-times the length of the spot itself, depending on the pressure gradient. In this case the observable calmed region is shorter than one spot length which could be partly due to the uncertainties of the heat flux determination. The heat flux intensifies throughout the spot, and reaches its maximum towards its trailing edge. This finding agrees well with the findings of Hogendoorn et al. [71], who examined the heat flux of turbulent spots for flow at $M = 0.33$. It is also in line with the expected wall shear stress increase towards the trailing edge [68].

Fig. 18 shows the surface temperature and heat flux temporal development for the turbulent spot presented above at one location ($x = 0.1$ m and $y = 0.168$ m). An uncertainty range for the presented values can be estimated by evaluating the standard deviation of the values for a time range with no turbulent spots and short enough for the heat flux and surface temperature to be approximately constant ($\Delta t < 0.01$ s — compare Fig. 9). Evaluating the time range $3.1\,\text{s} \leq t \leq 3.11\,\text{s}$ yields a standard deviation of $\sigma_{\dot{q}_w} = 1.6\,\text{kW/m}^2$ and $\sigma_T = 0.016\,\text{K}$.

The location of the trailing edge of the turbulent spot correlates with the minimum of the temperature distribution. The four consecutive

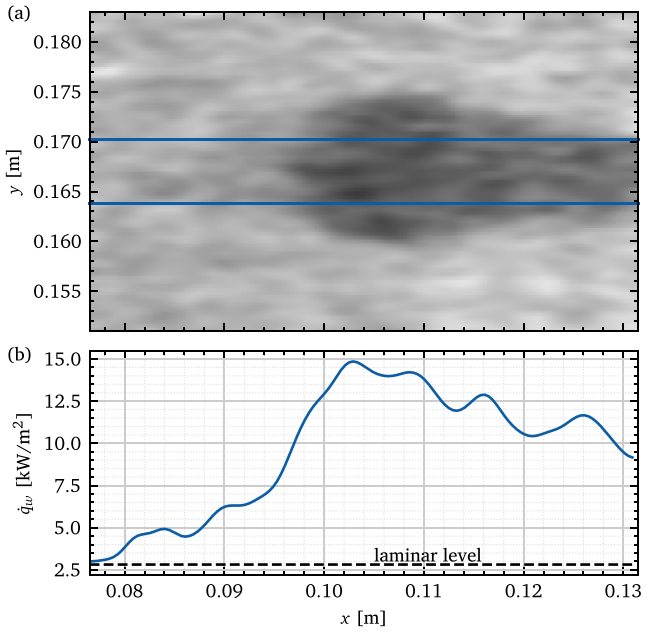

Fig. 17. Streamwise heat flux distribution for a turbulent spot presented in Fig. 16 with $Re_c = 6 \cdot 10^6$, $M = 0.8$, and $\lambda_\theta = 19.0 \cdot 10^{-3}$ at $t = 3.294\,25$ s. Colourmap as in Fig. 16. The streamwise distribution in (b) is averaged between the two blue lines indicated in (a). Flow is from the left.

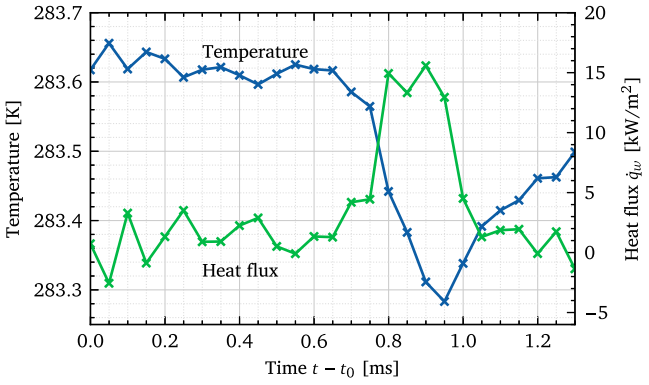

Fig. 18. Heat flux (green) and temperature (blue) temporal development for the turbulent spot previously presented with $Re_c = 6 \cdot 10^6$, $M = 0.8$, and $\lambda_\theta = 19.0 \cdot 10^{-3}$ at $x = 0.1$ m and $y = 0.168$ m and $t_0 = 3.2936$ s.

data points representing the inside of the turbulent spot ($3.2944\,\text{s} \leq t \leq 3.294\,55\,\text{s}$), corresponding to four separate image snapshots, have a roughly constant heat flux, the maximum being towards the end of the spot. Due to the high noise floor in the heat flux signal, the calmed region is not clearly distinguishable here.

4.2.2. Comparison with hot films

Fig. 19 shows the quasi wall shear stress τ_q for a typical example of a turbulent spot recorded with hot-film sensor 3 for flow conditions $Re_c = 6 \cdot 10^6$, $M = 0.8$, and $\lambda_\theta = 19.0 \cdot 10^{-3}$. As the leading edge arrives, τ_q increases sharply from its laminar level until it reaches its turbulent level, which indicates the turbulent spot has eventually covered the whole extent of the hot-film sensor. The gradient of τ_q occurs since it takes some time for the turbulent spot to cover the whole spanwise extent of the sensor. In this case, the turbulent spot covers the sensor for about $t = 0.22$ ms, during which time τ_q steadily increases. While this is to some extent expected, as mentioned above, the magnitude

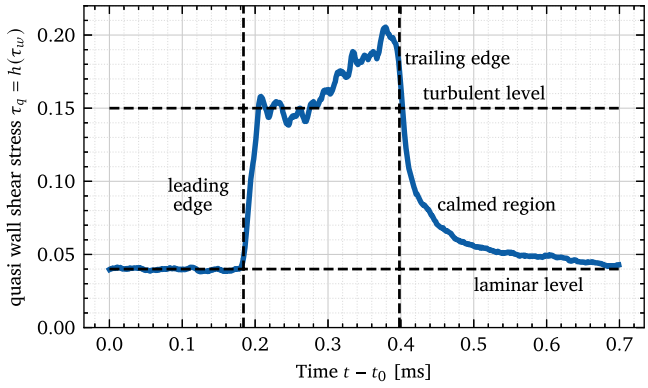

Fig. 19. Sample turbulent spot recorded with hot-film sensor 3 at $t_0 = 3.2812$ s. Flow conditions are $Re_c = 6 \cdot 10^6$, $M = 0.8$, and $\lambda_\theta = 19.0 \cdot 10^{-3}$.

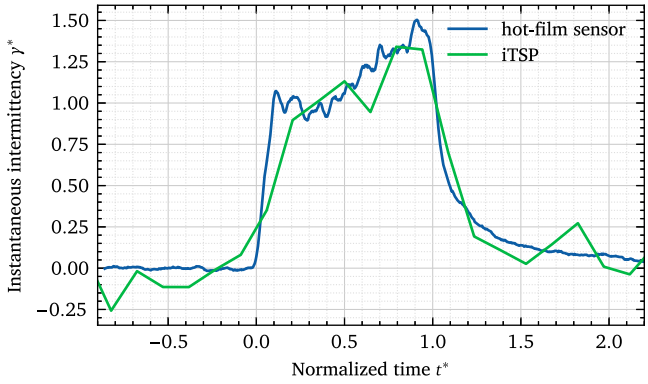

Fig. 20. Comparison of two independent turbulent spot traces recorded with hot-film sensor 3 (quasi wall shear stress — see Fig. 19) and iTSP at $x = 0.12$ m, $y = 0.168$ m (heat flux — see Fig. 16). Flow conditions are $Re_c = 6 \cdot 10^6$, $M = 0.8$, and $\lambda_\theta = 19.0 \cdot 10^{-3}$.

is surprising, as τ_q increases around 30 % during the passage of the spot. This increase is considerably more than observed, for example, by Hogendoorn et al. [71] in a flow at $M = 0.33$ (increase of 15 % to 20 %) and may therefore be partly explained with the uncertainty concerning the determination and accuracy of the quasi wall shear stress pointed out in Section 3.3. One further aspect is the increased heat flux of leads and carrier material in the vicinity of the sensor, which increases its total heat transfer with a temporal delay, promoted by the comparably high over-heat ratio to achieve the desired temporal resolution.

Fig. 20 illustrates the comparison of the quasi wall shear stress of the turbulent spot presented in Fig. 19 (spot passage time 0.22 ms) and the heat flux of a separate turbulent spot recorded with iTSP (spot passage time 0.34 ms) for the same flow conditions. The time is normalized with the time interval from leading to trailing edge passage of the spot, t_{le} and t_{te} respectively, $t^* = (t - t_{le})/(t_{le} - t_{te})$. The instantaneous intermittency γ^* is the respective signal with the laminar level set to 0 and the turbulent level set to 1. Although not representing the same turbulent spot, both methods yield the same overall characteristics, including the increased value towards the trailing edge of the spot. The calmed regions following the respective turbulent spots are clearly visible. They extend considerably longer than the spot duration itself for the spot recorded with the hot-film and contributes a significant amount to the total quasi wall shear stress caused by the turbulent spot. A similar behaviour is seen for the iTSP measurements, although the signal-to-noise ratio is lower.

5. Summary and outlook

This study used time-resolved temperature-sensitive paint (iTSP) to investigate transitional phenomena at high chord Reynolds numbers and high subsonic Mach numbers under favourable pressure gradients. A thin iTSP active layer enabled an acquisition rate of 20 kHz, for the first time providing the necessary temporal resolution to investigate unsteady transitional phenomena under these flow conditions. Assuming a 1D heat-transfer, it was possible to determine the surface heat flux based on the time-resolved surface temperature time series. A binary distribution of surface heat flux values was found, which allowed the identification of laminar and turbulent boundary layer states. This enabled the direct determination of the spatially resolved intermittency distribution for the observation area. In a streamwise direction the intermittency distribution was found to agree well with the theoretical distribution proposed by Johnson & Fashifar [19]. The transition locations obtained by determining the maximum gradient of the surface temperature in streamwise direction and the location of the highest temperature (temporal) standard deviation were confirmed to be in excellent agreement with the location of 50 % intermittency; their difference was mostly well below 2 mm in streamwise direction. Similarly, the intermittency distributions obtained with hot films were in good qualitative agreement with those from the iTSP data analysis, although a direct comparison was not possible because the iTSP and hot films were situated on different parts of the wind tunnel model. The high temporal and spatial resolution of the iTSP made it possible to observe and characterize individual turbulent spots. The heat flux level obtained with iTSP and the quasi wall shear stress determined with the hot films increase towards the trailing edge of the spot, and a calmed region following the spot could be observed.

The results demonstrate the capabilities of time-resolved temperature-sensitive paint to non-intrusively capture unsteady phenomena at the examined high Reynolds number flow conditions, due to its high temporal and spatial resolution. It can be used in future to further investigate transitional phenomena, which includes specific aspects such as properties of turbulent spots or the influence of flow parameters on transition location and length. Furthermore, the determination of time-resolved surface heat flux is of great benefit for numerous applications such as hypersonic flight or turbomachinery flows.

CRediT authorship contribution statement

Benjamin Dimond: Writing – review & editing, Writing – original draft, Visualization, Validation, Software, Resources, Project administration, Methodology, Investigation, Formal analysis, Data curation, Conceptualization. **Marco Costantini:** Writing – review & editing, Validation, Supervision, Resources, Project administration, Methodology, Investigation, Conceptualization. **Christian Klein:** Writing – review & editing, Validation, Supervision, Resources, Project administration, Methodology, Funding acquisition, Conceptualization.

Declaration of generative AI in scientific writing

Generative AI was not used in this article.

Funding sources

This research did not receive any specific grant from funding agencies in the public, commercial, or not-for-profit sectors.

Declaration of competing interest

The authors declare that they have no known competing financial interests or personal relationships that could have appeared to influence the work reported in this paper.

Acknowledgements

The Authors would like to thank S. Koch, M. Aschoff and S. Weiss for wind tunnel operation, C. Fuchs, T. Hermann, K. Kienass, T. Kleindienst, S. Roth, and H. Böhlken for model preparation and instrumentation and experimental setup. We are grateful to U. Henne for support with data acquisition and S. Risius for paving the way towards this experimental setup by implementing a periscope and the PaLASTra model aft part in preceding investigations. Furthermore we thank M. Rein for valuable discussion of the results and W. Beck for support in preparation of the manuscript.

Appendix A. Heat flux calculations

Eq. (9) is solved numerically with the method of lines based on the finite-difference method with a forward differential in time and central differential in space with location node i and time instance n. With

$$\kappa = \alpha_{max}\frac{\Delta t}{\Delta z^2}, \tag{A.1}$$

where α_{max} corresponds to the maximum thermal diffusivity ($\alpha = k/(\rho c)$) of the layers, the temperature at a given location node i and time instance $n+1$ is only dependent on its node and neighbouring nodes at time instance n:

$$\rho_i c_i \frac{T_i^{n+1} - T_i^n}{\Delta t} = \frac{1}{\Delta z^2}\left[k_{i+1/2}T_{i+1}^n - (k_{i+1/2} + k_{i-1/2})T_i^n + k_{i-1/2}T_{i-1}^n\right] \tag{A.2}$$

$$\Rightarrow \quad T_i^{n+1} = \kappa\left[\alpha_{i+1/2}T_{i+1}^n - \left(\alpha_{i+1/2} + \alpha_{i-1/2}\right)T_i^n + \alpha_{i-1/2}T_{i-1}^n\right] + T_i^n \tag{A.3}$$

where

$$\alpha_{i+1/2} := \frac{k_{i+1} + k_i}{2\rho_i c_i \alpha_{max}} \tag{A.4}$$

$$\alpha_{i-1/2} := \frac{k_i + k_{i-1}}{2\rho_i c_i \alpha_{max}}. \tag{A.5}$$

Since the thermal properties are not defined at the interface of the different layers, but are considered constant within a layer, $\alpha_{i+1/2}$ and $\alpha_{i-1/2}$ are set to be the values corresponding to the value of the material at node $i+1$ and $i-1$, respectively. Note that this is a simplification, since it ignores the thermal contact resistance and assumes perfect heat transfer between two layers. This simplification is nevertheless reasonable, since the layers are spray painted, which reduces their thermal contact resistance compared to two touching solids. To enable a sufficiently small spatial resolution, a cubic interpolation of temperature data is performed in time.

The result of the preceding numerical calculation is then used to determine the heat flux according to Eq. (10) with the time-resolved temperature values of two neighbouring grid points in z-direction at the surface (T_1^t and T_0^t) and the thermal conductivity of the base layer ($k = k_b$):

$$\dot{q}_w(t) = -k_b\frac{T_1^t - T_0^t}{\Delta z} \tag{A.6}$$

Based on values provided in Ozawa et al. [31], an estimate for the thermal conductivity of the base layer is given by $k_b = 0.202(16)\,\mathrm{W/(m\cdot K)}$, but this value varies in other publications.

Table A.1
Thermal diffusivity for the materials relevant to calculate the heat flux.

Material	Thermal diffusivity α [m^2/s]
Maraging steel (1.6359) (Manufacturer information)	$5.67 \cdot 10^{-6}$
Primer layer [72]	$5.8 \cdot 10^{-6}$
Base layer [31]	$1.09 \cdot 10^{-7}$

The simplification of using a one-dimensional approximation is justified as the temperature gradient in the streamwise direction on the surface is much lower than the temperature gradient toward the inside of the model. For a typical case, this difference is more than two orders of magnitude (0.4 K/mm compared to 50 K/mm) in the region of 50 % intermittency, and even more outside this region. Therefore, expanding the calculations to a full 3D model is not expected to alter the results significantly. However, this assumption may not be valid for a much thinner base layer than considered here, or for longer times.

The thermal properties of thin layers are not easy to determine. They can vary depending on the thickness of the layer and depend on the layer interfaces, as these can have a significant influence on the thermal diffusivity. Table A.1 lists the thermal diffusivities α used to determine the heat flux. The most important value is that of the base layer, as this contains the largest temperature gradient over its thickness. However, several differing values are reported in literature, determined directly and through in-situ calibration [31,54].

Abbreviations

CMOS	Complementary Metal-Oxide-Semiconductor
COCO	Compressible flow boundary layer solver
iTSP	fast-response Temperature-Sensitive Paint
KRG	Cryogenic Ludwieg-Tube Göttingen
LED	Light-Emitting Diode
MHFS	Multiple Hot-Film Sensor array
PaLASTra	Test model name: flat Plate for the Analysis of the effect on LAminar-turbulent transition of Surface imperfections, wall Temperature ratio and pressure gRAdient
ToPas	Three-dimensional optical Pressures analysis system
TSP	Temperature-Sensitive Paint

Latin letters

$\dot{q}_w^*$	Non-dimensional surface heat flux
$\dot{q}_w$	Surface heat flux (W/m^2)
c_p	Specific heat capacity at constant pressure (J/kg K)
c_{le}, c_{te}	Leading and trailing edge celerity of turbulent spots (m/s)
c	Chord length (m)
$g(P_0)$	Spot production function at point P_0
I_+, I_-	Intensity at temperature $T + \Delta T$ or $T - \Delta T$
I	Luminescent intensity
k	Thermal conductivity (W/m K)
M	Mach number, based on freestream velocity and freestream speed of sound
n	Turbulent spot production rate per unit length (1/m)
Re_c	Chord Reynolds number, based on chord length, freestream velocity, and freestream kinematic viscosity
R	Dependence volume (spot sweep volume), Resistance (Ω)
S	Temperature sensitivity of TSP (%/K)
T^*	Non-dimensional surface temperature
T_w	Surface temperature (K)
T_{aw}	Adiabatic wall temperature (K)
t	Time (s)
$U(t)$	Hot-film voltage during run
U_0	Hot-film voltage without flow
U_∞	Freestream velocity (m/s)
x_{25}, x_{75}	Streamwise locations with $\gamma = 0.25$ and $\gamma = 0.75$
$x_{g,max}$	Streamwise location of maximum spot production
x	Streamwise coordinate (m)
y	Spanwise coordinate (m)
z	Wall-normal coordinate (m)

Greek letters

α	Spot spreading angle (rad), Thermal diffusivity (m^2/s)
γ	Intermittency factor
κ	$\alpha_{max} \frac{\Delta t}{\Delta z^2}$
λ_θ	Streamwise pressure gradient parameter
ν	Kinematic viscosity (m^2/s)
ρ	Density (kg/m^3)
σ_T	Standard deviation of surface temperature over time
σ	Emmons' dimensionless spot propagation parameter
τ_q	Quasi wall shear stress (non-dimensional)
θ	Momentum thickness (m)
ξ	Dimensionless streamwise coordinate

Appendix B. Supplementary data

Supplementary material related to this article can be found online at https://doi.org/10.1016/j.expthermflusci.2026.111781.

Data availability

Data will be made available on request.

References

[1] R.D. Joslin, Overview of Laminar Flow Control, Tech. Rep., Langley Research Center, Hampton, Virginia, 1998.

[2] R.E. Mayle, The 1991 IGTI scholar lecture: The role of laminar-turbulent transition in gas turbine engines, J. Turbomach. 113 (4) (1991) 509–536, http://dx.doi.org/10.1115/1.2929110.

[3] A. Fedorov, Transition and stability of high-speed boundary layers, Annu. Rev. Fluid Mech. 43 (1) (2011) 79–95, http://dx.doi.org/10.1146/annurev-fluid-122109-160750.

[4] F.M. White, J. Majdalani, Viscous Fluid Flow, vol. 3, McGraw-Hill New York, 2006.

[5] W.S. Saric, A.S.W. Thomas, Experiments on the subharmonic route to turbulence in boundary layers, Turbul. Chaotic Phenom. Fluids (1984) 117–122.

[6] J.W. Elder, An experimental investigation of turbulent spots and breakdown to turbulence, J. Fluid Mech. 9 (1960) 235–246, http://dx.doi.org/10.1017/s0022112060001079.

[7] H.W. Emmons, The laminar-turbulent transition in a boundary layer - Part I, J. Aeronaut. Sci. 18 (1951) 490–498, http://dx.doi.org/10.2514/8.2010.

[8] S. Dhawan, R. Narasimha, Some properties of boundary layer flow during the transition from laminar to turbulent motion, J. Fluid Mech. 3 (1958) 418–436, http://dx.doi.org/10.1017/S0022112058000094.

[9] J.P. Gostelow, A.R. Blunden, Investigations of boundary layer transition in an adverse pressure gradient, J. Turbomach. 111 (4) (1989) 366–374, http://dx.doi.org/10.1115/1.3262281.

[10] G.J. Walker, J.P. Gostelow, Effects of adverse pressure gradients on the nature and length of boundary layer transition, J. Turbomach. 112 (2) (1990) 196–205, http://dx.doi.org/10.1115/1.2927633.

[11] R.G. N. Vinod, Pattern of breakdown of laminar flow into turbulent spots, Phys. Rev. Lett. 93 (2004) 114501, http://dx.doi.org/10.1103/PhysRevLett.93.114501.

[12] J.P. Gostelow, N. Melwani, G.J. Walker, Effects of streamwise pressure gradient on turbulent spot development, J. Turbomach. 118 (1996) 737–743, http://dx.doi.org/10.1115/1.2840929.

[13] J.S. Jewell, I.A. Leyva, J.E. Shepherd, Turbulent spots in hypervelocity flow, Exp. Fluids 58 (2017) 1–14, http://dx.doi.org/10.1007/s00348-017-2317-y.

[14] R. Narasimha, The laminar-turbulent transition zone in the boundary layer, Prog. Aerosp. Sci. 22 (1985) 29–80, http://dx.doi.org/10.1016/0376-0421(85)90004-1.

[15] R. Narasimha, Modelling the Transitional Boundary Layer, Tech. Rep., NASA, 1990.

[16] D.J. Mee, C.P. Goyne, Turbulent spots in boundary layers in a free-piston shock-tunnel flow, Shock Waves 6 (1996) 337–343, http://dx.doi.org/10.1007/BF02511324.

[17] F.K. Owen, Transition experiments on a flat plate at subsonic and supersonic speeds, AIAA J. 8 (3) (1970) 518–523, http://dx.doi.org/10.2514/3.5699.

[18] L. Krishnan, N.D. Sandham, Effect of Mach number on the structure of turbulent spots, J. Fluid Mech. 566 (2006) 225–234, http://dx.doi.org/10.1017/S0022112006002412.

[19] M.W. Johnson, A. Fashifar, Statistical properties of turbulent bursts in transitional boundary layers, Int. J. Heat Fluid Flow 15 (1994) 283–290, http://dx.doi.org/10.1016/0142-727X(94)90013-2.

[20] B.J. Abu-Ghannam, R. Shaw, Natural transition of boundary layers—the effects of turbulence, pressure gradient, and flow history, J. Mech. Eng. Sci. 22 (1980) 213–228, http://dx.doi.org/10.1243/jmes_jour_1980_022_043_02.

[21] J.H.M. Fransson, M. Matsubara, P.H. Alfredsson, Transition induced by free-stream turbulence, J. Fluid Mech. 527 (2005) 1–25, http://dx.doi.org/10.1017/s0022112004002770.

[22] S. Shahinfar, J.H.M. Fransson, Effect of free-stream turbulence characteristics on boundary layer transition, in: Journal of Physics: Conference Series, Vol. 318, IOP Publishing, 2011, 032019, http://dx.doi.org/10.1088/1742-6596/318/3/032019.

[23] M. Costantini, Experimental Analysis of Geometric, Pressure Gradient and Surface Temperature Effects on Boundary-Layer Transition in Compressible High Reynolds Number Flows (Ph.D. thesis), RWTH Aachen, 2016.

[24] B. Dimond, Investigation of Boundary Layer Transition at High Reynolds Numbers Using Time-Resolved Temperature-Sensitive Paint (Ph.D. thesis), Georg-August-University Göttingen, 2024, http://dx.doi.org/10.53846/goediss-10693.

[25] T. Liu, J.P. Sullivan, K. Asai, C. Klein, Y. Egami, Pressure and Temperature Sensitive Paints, second ed., Experimental Fluid Mechanics, Springer, 2021, http://dx.doi.org/10.1007/978-3-030-68056-5.

[26] M. Costantini, S. Risius, C. Klein, Experimental investigation of the effect of forward-facing steps on boundary layer transition, Procedia IUTAM 14 (2015) 152–162, http://dx.doi.org/10.1016/j.piutam.2015.03.036.

[27] B. Dimond, M. Costantini, S. Risius, C. Fuchs, C. Klein, Experimental analysis of suction on step-induced boundary-layer transition, Exp. Therm. Fluid Sci. 109 (2019) 109842.

[28] M. Miozzi, A. Capone, M. Costantini, L. Fratto, C. Klein, F. Di Felice, Skin friction and coherent structures within a laminar separation bubble, Exp. Fluids 60 (2019) 1–25, http://dx.doi.org/10.1007/s00348-018-2651-8.

[29] S. Risius, M. Costantini, S. Koch, S. Hein, C. Klein, Unit Reynolds number, Mach number and pressure gradient effects on laminar–turbulent transition in two-dimensional boundary layers, Exp. Fluids 59 (2018) 1–29, http://dx.doi.org/10.1007/s00348-018-2538-8.

[30] J. Martinez Schramm, M. Hilfer, Time response calibration of ultra-fast temperature sensitive paints for the application in high temperature hypersonic flows, in: New Results in Numerical and Experimental Fluid Mechanics XII: Contributions To the 21st STAB/DGLR Symposium, Darmstadt, Germany, 2018, Springer, 2020, pp. 143–152, http://dx.doi.org/10.1007/978-3-030-25253-3_14.

[31] H. Ozawa, S.J. Laurence, J. Martinez Schramm, A. Wagner, K. Hannemann, Fast-response temperature-sensitive-paint measurements on a hypersonic transition cone, Exp. Fluids 56 (2015) 1853, http://dx.doi.org/10.1007/s00348-014-1853-y.

[32] H. Ozawa, S.J. Laurence, Experimental investigation of the shock-induced flow over a wall-mounted cylinder, J. Fluid Mech. 849 (2018) 1009–1042, http://dx.doi.org/10.1017/jfm.2018.433.

[33] J. Jung, S. Saito, S. Someya, S. Baba, N. Takada, Fabrication of thin inorganic temperature-sensitive paint using ball milling and its temporal response delay, Meas. Sci. Technol. 35 (6) (2024) http://dx.doi.org/10.1088/1361-6501/ad30b9.

[34] X. Liu, Y. Zhuang, Y. Zhang, G. Wang, Y. Liu, D. Peng, Time-resolved heat flux determination from fast-responding temperature-sensitive paint measurement in a shock tunnel using transient in-situ calibration, Meas. Sci. Technol. 35 (3) (2023) http://dx.doi.org/10.1088/1361-6501/ad13e6.

[35] D.L. Schultz, T.V. Jones, Heat-transfer measurements in short-duration hypersonic facilities, in: AGARD AG-165, Agard, 1973.

[36] A. Petersen, B. Dimond, A.-S. Söhngen, F. Süß, A. Ebach-Stahl, R. Naraparaju, M. Hilfer, R.G. Brakmann, Wind tunnel testing at TRL4 of EBC-coated SIC/SIC nozzle guide vanes for high-pressure turbines with trailing edge cooling, J. Turbomach. 148 (5) (2026) 051016, http://dx.doi.org/10.1115/1.4070234.

[37] B. Dimond, M. Costantini, C. Klein, Investigation of turbulent wedge intermittency with time-resolved temperature-sensitive paint, in: IUTAM Laminar-Turbulent Transition: 10th IUTAM Symposium, Springer Nature Link, 2026, pp. 47–53, http://dx.doi.org/10.1007/978-981-96-9829-5_7.

[38] K. Yoshikawa, H. Ozawa, Heat transfer visualization of transitional growth of turbulent spot on a wedge in Mach 5.2 hypersonic flow using fast-response TSP, Exp. Fluids 66 (2) (2025) 30, http://dx.doi.org/10.1007/s00348-025-03964-8.

[39] S. Koch, Zeitliche und Räumliche Turbulenzentwicklung in Einem Rohrwindkanal Und Deren Einfluss Auf Die Transition an Profilmodellen (Ph.D. thesis), Institute of Aerodynamics and Flow Technology, DLR Goettingen, 2004.

[40] M. Costantini, S. Hein, U. Henne, C. Klein, S. Koch, L. Schojda, V. Ondrus, W. Schröder, Pressure gradient and nonadiabatic surface effects on boundary layer transition, AIAA J. 54 (11) (2016) 3465–3480, http://dx.doi.org/10.2514/1.j054583.

[41] H. Rosemann, The Cryogenic Ludwieg-tube Tunnel at Gottingen, 1996, pp. 8–1 to 8–13, AGARD-R-812.

[42] N. Lin, H.L. Reed, W. Saric, Effect of leading-edge geometry on boundary-layer receptivity to freestream sound, in: Instability, Transition, and Turbulence, Springer, 1992, pp. 421–440, http://dx.doi.org/10.1007/978-1-4612-2956-8_42.

[43] G. Schrauf, COCO - A Program to Compute Velocity and Temperature Profiles for Local and Nonlocal Stability Analysis of Compressible, Conical Boundary Layers with Suction, Zarm Technik report, Bremen, Germany, 1998.

[44] B. Dimond, M. Costantini, C. Klein, Experimental analysis of the effect of suction and step height on boundary-layer transition, in: IUTAM Laminar-Turbulent Transition: 9th IUTAM Symposium, London, UK, September 2–6, 2019, Springer, 2022, pp. 171–180, http://dx.doi.org/10.1016/j.expthermflusci.2019.109842.

[45] V. Ondrus, R.J. Meier, C. Klein, U. Henne, M. Schäferling, U. Beifuss, Europium 1,3-di(thienyl)propane-1,3-diones with outstanding properties for temperature sensing, Sensors Actuators A 233 (2015) 434–441, http://dx.doi.org/10.1016/j.sna.2015.07.023.

[46] C. Klein, R. Engler, U. Henne, W. Sachs, Application of pressure-sensitive paint for determination of the pressure field and calculation of the forces and moments of models in a wind tunnel, Exp. Fluids 39 (2005) 475–483, http://dx.doi.org/10.1007/s00348-005-1010-8.

[47] A. Mills, Optical oxygen sensors utilising the luminescence of platinum metal complexes, Platinum Met. Rev. 41 (1997) 115–127, http://dx.doi.org/10.1595/003214097x413115127.

[48] H. Ozawa, Experimental study of unsteady aerothermodynamic phenomena on shock-tube wall using fast-response temperature-sensitive paints, Phys. Fluids 28 (2016) http://dx.doi.org/10.1063/1.4947040.

[49] M. Bitter, M. Hilfer, T. Schubert, C. Klein, R. Niehuis, An ultra-fast TSP on a CNT heating layer for unsteady temperature and heat flux measurements in subsonic flows, Sensors 22 (2) (2022) http://dx.doi.org/10.3390/s22020657.

[50] A. Petersen, M. Hilfer, Boundary layer analysis of a transonic high-pressure turbine vane using ultra-fast-response temperature-sensitive paint, in: Turbo Expo: Power for Land, Sea, and Air, Vol. 87110, American Society of Mechanical Engineers, 2023, V13DT36A007, http://dx.doi.org/10.1115/1.4065739.

[51] Y. Egami, U. Fey, C. Klein, J. Quest, V. Ondrus, U. Beifuss, Development of new two-component temperature-sensitive paint (TSP) for cryogenic testing, Meas. Sci. Technol. 23 (2012) 115301, http://dx.doi.org/10.1088/0957-0233/23/11/115301.

[52] S. Risius, M. Costantini, S. Hein, S. Koch, C. Klein, Experimental investigation of Mach number and pressure gradient effects on boundary layer transition in two-dimensional flow, in: New Results in Numerical and Experimental Fluid Mechanics XI, Springer, 2018, pp. 305–314, http://dx.doi.org/10.1007/978-3-319-64519-3_28.

[53] S. Risius, Development of a Time-Resolved Quantitative Surface-Temperature Measurement Technique and its Application in Short-Duration Wind Tunnel Testing (Ph.D. thesis), Georg-August-Universität Göttingen, 2018, http://dx.doi.org/10.53846/goediss-6963.

[54] S. Risius, W.H. Beck, C. Klein, U. Henne, A. Wagner, Determination of heat transfer into a wedge model in a hypersonic flow using temperature-sensitive paint, Exp. Fluids 58 (2017) 1–13, http://dx.doi.org/10.1007/s00348-017-2393-z.

[55] S.J. Laurence, H. Ozawa, J. Martinez Schramm, C.S. Butler, K. Hannemann, Heat-flux measurements on a hypersonic inlet ramp using fast-response temperature-sensitive paint, Exp. Fluids 60 (2019) 1–16, http://dx.doi.org/10.1007/s00348-019-2711-8.

[56] E. Schülein, Skin friction and heat flux measurements in shock/boundary layer interaction flows, AIAA J. 44 (8) (2006) 1732–1741, http://dx.doi.org/10.2514/1.15110.

[57] T.L. Bergman, A.S. Lavine, F.P. Incropera, D.P. Dewitt, Fundamentals of Heat and Mass Transfer, vol. 7, John Wiley & Sons, 2011.

[58] N. Otsu, A threshold selection method from gray-level histograms, IEEE Trans. Syst. Man Cybern. 9 (1979) 62–66, http://dx.doi.org/10.1109/tsmc.1979.4310076.

[59] H.P. Hodson, I. Huntsman, A.B. Steele, An investigation of boundary layer development in a multistage LP turbine, J. Turbomach. (1994) http://dx.doi.org/10.1115/1.2929424.

[60] M. Braune, S. Koch, Application of hot-film anemometry to resolve the unsteady boundary layer transition of a laminar airfoil experiencing limit cycle oscillations, Exp. Fluids 61 (2) (2020) 68, http://dx.doi.org/10.1007/s00348-020-2907-y.

[61] J.P. Clark, P. Magari, T.V. Jones, J.E. Lagraff, Experimental studies of turbulent spot parameters using thin-film heat-transfer gauges, in: 31st Aerospace Sciences Meeting & Exhibit, Vol. 544, 1993, http://dx.doi.org/10.2514/6.1993-544.

[62] P. Ashill, C. Betts, I. Gaudet, A wind tunnel study of transition flows on a swept panel wing at high subsonic speeds, in: CEAS 2nd European Forum on Laminar Flow Technology, Vol. 10, 1996, pp. 1–17.

[63] M. Costantini, U. Henne, S. Risius, C. Klein, A robust method for reliable transition detection in temperature-sensitive paint data, Aerosp. Sci. Technol. 113 (2021) 106702, http://dx.doi.org/10.1016/j.ast.2021.106702.

[64] D. Arnal, G. Casalis, R. Houdeville, Practical Transition Prediction Methods: Subsonic and Transonic Flows, VKI Lectures Series Advances in Laminar-Turbulent Transition Modelling, 2008.

[65] H.-P. Kreplin, G. Höhler, Application of the surface hot film technique for laminar flow investigations, in: Proc. 1st European Forum on Laminar Flow Technology, Deutsche Gesellschaft für Luft- und Raumfahrt - Lilienthal-Oberth e.V., Bonn, Germany, 1992, pp. 123–131.
[66] K.K. Chen, N.A. Thyson, Extension of Emmons' spot theory to flows on blunt bodies, AIAA J. 9 (5) (1971) 821–825, http://dx.doi.org/10.2514/3.6281.
[67] A. Weiss, A.D. Gardner, C. Klein, M. Raffel, Boundary-layer transition measurements on Mach-scaled helicopter rotor blades in climb, CEAS Aeronaut. J. 8 (4) (2017) 613–623, http://dx.doi.org/10.1007/s13272-017-0263-2.
[68] I. Wygnanski, M. Sokolov, D. Friedman, On a turbulent 'spot' in a laminar boundary layer, J. Fluid Mech. 78 (1976) 785–819, http://dx.doi.org/10.1017/S0022112076002747.
[69] R.E. Mayle, M. Stripf, "I-Spots" and Emmons' spot production rate, J. Turbomach. 143 (2021) 091019, http://dx.doi.org/10.1115/1.4051105.
[70] B.F.A. Van Hest, D.M. Passchier, J.L. van Ingen, The development of a turbulent spot in an adverse pressure gradient boundary layer, in: R. Kobayashi (Ed.), Laminar-Turbulent Transition, Springer Berlin Heidelberg, Berlin, Heidelberg, 1995, pp. 255–262, http://dx.doi.org/10.1007/978-3-642-79765-1_30.
[71] C.J. Hogendoorn, H.C. de Lange, A.A. van Steenhoven, Design optimization for fast heat-transfer gauges, Meas. Sci. Technol. 9 (1998) 428–434, http://dx.doi.org/10.1088/0957-0233/9/3/017.
[72] R. Sottong, Private communication, 2015.